Effects of Donor Position and Multiple Charge Transfer Pathways in Asymmetric Pyridyl-Sulfonyl TADF Emitters

Gulcin Haykir, Murat Aydemir, Adem Tekin, Emine Tekin, Andrew Danos, Fatma Yuksel, Gurkan Hizal, Andrew P. Monkman, Figen Turksoy

PII: S2352-4928(22)00417-2

DOI: https://doi.org/10.1016/j.mtcomm.2022.103550

Reference: MTCOMM103550

To appear in: *Materials Today Communications*

Received date: 31 December 2021
Revised date: 31 March 2022
Accepted date: 12 April 2022

Please cite this article as: Gulcin Haykir, Murat Aydemir, Adem Tekin, Emine Tekin, Andrew Danos, Fatma Yuksel, Gurkan Hizal, Andrew P. Monkman and Figen Turksoy, Effects of Donor Position and Multiple Charge Transfer Pathways in Asymmetric Pyridyl-Sulfonyl TADF Emitters, *Materials Today Communications,* (2021) doi:https://doi.org/10.1016/j.mtcomm.2022.103550

Effects of Donor Position and Multiple Charge Transfer Pathways in Asymmetric Pyridyl-Sulfonyl TADF Emitters

Gulcin Haykir,[a,b] Murat Aydemir,[c,d*] Adem Tekin,[e,f] Emine Tekin,[g] Andrew Danos,[d] Fatma Yuksel,[h] Gurkan Hizal,[b] Andrew P. Monkman[d] and Figen Turksoy [a*]

[a]TUBITAK Marmara Research Center, Institute of Chemical Technology, p.b. 21, 41470, Gebze,Turkey.
[b] Department of Chemistry, Istanbul Technical University, Maslak, 34469, Istanbul, Turkey.
[c] Department of Fundamental Sciences, Faculty of Science, Erzurum Technical University, Erzurum, Turkey.
[d] Physics Department, OEM Research Group, Durham University, Rochester Building, South Road, DH1 3LE County Durham, United Kingdom.
[e] Informatics Institute, Istanbul Technical University, 34469 Maslak, Istanbul, Turkey.
[f] TUBITAK Research Institute for Fundamental Sciences, 41470 Gebze, Kocaeli, Turkey.
[g] TUBITAK Marmara Research Center, Material Institute, p.b. 21, 41470, Gebze,Turkey.
[h] Department of Chemistry, Gebze Institute of Technology, Gebze 41400, Kocaeli, Turkey.

Highlights:

- We report the synthesis and structural characterization of D-aA-D' type pyridyl-sulfonyl based isomers comprising the phenothiazine and carbazole donor units, which are able to emit thermally activated delayed fluorescence
- The isomer with *para*- phenothiazine group displays significantly improved delayed fluorescence and emission quantum yields
- Both materials exhibit warm-yellowish emission in non-doped OLEDs with CIE coordinates of (0.41; 0.53, 0.49; 0.48) and maximum EQEs of 0.5% (*meta*- isomer) and 1.9% (*para*- isomer)

TOC Graphic

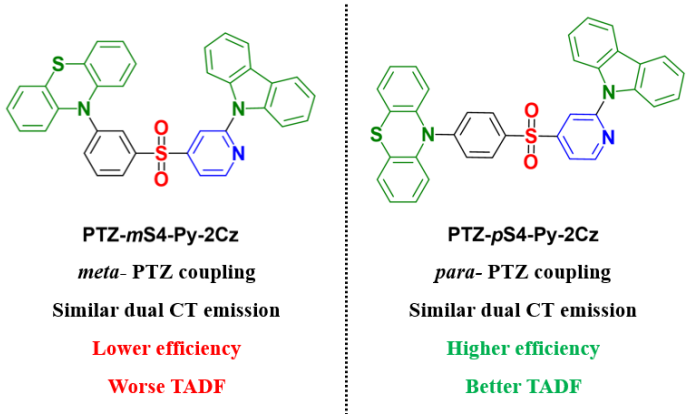

Abstract

We have designed and synthesized a pair of highly asymmetric D-aA-D' type pyridyl-sulfonyl based isomers comprising phenothiazine (PTZ) and carbazole (Cz) donor units, which are able to emit thermally activated delayed fluorescence. **PTZ-*p*S4-Py-2Cz** and **PTZ-*m*S4-Py-2Cz** both possess spatial separation of HOMO/LUMO on the donor and acceptor moieties, resulting in small calculated singlet–triplet energy gaps (~0.25 eV). Both isomers exhibit dual emission, which is attributed to charge transfer states associated with the Cz and PTZ moieties at higher and lower energies, respectively. Photoluminescence quantum yields and time-resolved emission decays show significant differences for the two isomers, with the *para*- isomer exhibiting more efficient emission and stronger delayed fluorescence than the *meta*- isomer – in strong contrast to recently reported analogous Cz-Cz D-aA-D isomers. The findings clearly show that the interconversion of triplets via the rISC mechanism is promoted when parallel Cz and PTZ charge transfer states are allowed to interact, explaining the improved performance of the Cz-PTZ materials compared to the previous Cz-Cz ones. Finally, moderate device performance was achieved in warm-yellowish (CIE; 0.41; 0.53 & 0.49; 0.48) non-doped OLEDs, which exhibited 0.5% & 1.9% maximum external quantum efficiencies for the *meta*- and *para*-isomers, respectively.

Keywords:

Dual Emission, TADF, Phenothiazine & Carbazole

* corresponding authors

Introduction

Thermally activated delayed fluorescence (TADF) emitters have recently become the key materials used to progress third-generation organic light emitting diode (OLED) technologies. Theoretically, TADF materials can reach up to 100% internal quantum efficiency because all the electrically generated triplet excitons are capable of being converted to emissive singlet states[1–3]. This unique spin-conversion process called reverse intersystem crossing (rISC) requires spatial separation of HOMO/LUMO of donor and acceptor groups to achieve charge-transfer (CT) states small singlet–triplet energy gaps (ΔE_{ST})[4–6]. Towards this end, donor (D) and acceptor (A) groups with steric hindrance are commonly connected to optimise the

equilibrium geometry between them[7–9]. It is critical to choose suitable D and A functional groups while designing TADF emitters, as the efficiency of the resulting materials depends greatly upon the electron donating/accepting strengths as well as the bonding pattern within the larger molecule[10–13]. Furthermore, while highly perpendicular D-A geometries can enhance rISC, the same kinds of structures also lead to weak oscillator strengths and low photoluminescence quantum yields (PLQYs), requiring a compromise approach for optimum material performance[14–15].

Recently we have reported a set of asymmetric D-aA-D materials [10], which featured carbazole (Cz) donors in different positions. We found that the position of the auxiliary acceptor (a), in the mono- and disubstituted pyridine materials can strongly impact the TADF performance despite these materials all comprising identical D and Aa chemical groups. In different positioned pyridyl-sulfonyl derivatives, 2,4- substituted regioisomers were found to possess superior optical and physical properties. Simultaneously, the position of the Cz donor on the side of the molecule opposite to the pyridine group was found to have minimal effect on the TADF and PLQY properties for *meta*- and *para*- substitution.

Separately, we have also recently reported on the excited state properties of a related asymmetric D-A-D' TADF material, employing chemically distinct D and D' units [16]. In that work, it was demonstrated that the CT state associated with the stronger phenothiazine (PTZ) donor unit dominated the photophysical properties in (4-(9H-carbazol-9-yl)phenyl)(4-(10H-phenothiazin-10-yl)-phenyl)sulfone (SFPC) molecule, highlighted through comparison to the symmetric D-A-D and D'-A-D' materials.

Combining the concepts of both previous works, herein we present an effective design concept for TADF materials and examine the excited state properties of highly asymmetric D-aA-D' emitters **PTZ-*p*S4-Py-2Cz** and **PTZ-*m*S4-Py-2Cz** (Scheme 1). Based on the superior performance in the previous work, the 2,4- substituted pyridyl-sulfonyl structure was chosen as the asymmetric aA acceptor unit. D-Aa-D' structures were then obtained by coupling this to Cz, and to PTZ in two different isomer patterns. Comparison to previously studied PTZ and Cz analogy gives valuable context for understanding the unexpected optical behaviours of the new materials. For PTZ in particular, its geometric "butterfly wing" folding distortions enabled by the larger atomic radius of sulphur relative to oxygen[17,18], were expected to prevent molecular aggregation and provide high HOMO electron densities[19–22]. In both molecules we observe

dual CT emission with enhanced delayed fluorescence from the PTZ CT state. In both optical and device (non-doped OLEDs) measurements the *para*- isomer is found the have superior performance to the *meta*- isomer, in strong contrast to the near-identical performance of the analogous Cz-Cz materials.

2. Material and Methods

2.1. Synthesis Details

Materials

All reagents and solvents were obtained from commercial suppliers and used without further purification. Solvents were distilled using standard methods and purged with N_2 before use. All the experiments were carried out under N_2. Column chromatography was performed on silica gel 60 (230-400 mesh) and TLC was performed on silica gel 60 F_{254} alumina plates.

General Procedure for Ullmann Reaction

An oven-dried flask was charged with corresponding halogenated phenyl-sulfonyl pyridine derivatives (**9Ac** & **9Ac'**) (1.0 eq), 9H-carbazole (1.1 eq **9Ac** & **9Ac'**) and p-xylene. Then copper(I)iodide (11% of **9Ac** & **9Ac'**), 1,10-phenanthroline (11% of **9Ac** & **9Ac'**) and potassium carbonate (2.0 eq for **9Ac** & **9Ac'**) were added under nitrogen atmosphere respectively. The reaction mixture was refluxed for 48 h, at 138°C. After cooling to room temperature the mixture was extracted with dichloromethane (3 x 50 mL). Combined organic phases were then washed with brine and dried over Na_2SO_4. After the solvent was removed, the material was further purified with silica gel column chromatography using dichloromethane:hexane (2:1) eluent.

9-(4-(4-bromophenylsulfonyl)pyridin-2-yl)-9H-carbazole (Br-*p*S4-Py-2Cz)

The title compound was obtained from **9Ac** (0.6 g, 1.59 mmol) as off-white colored solid **Br-*p*S4-Py-2Cz** in 75% (0.55 g).

FTIR (KBr, cm^{-1}): 3453, 3079, 3056, 2923, 2851, 1622, 1596, 1573, 1490, 1478, 1465, 1449, 1403, 1389, 1334, 1322, 1275, 1248, 1215, 1189, 1150, 1106, 1068, 1077, 1030, 1009, 991, 970, 932, 913, 889, 855, 820, 790, 774, 752, 709, 655, 645, 625, 613, 576, 567, 536, 496. **^{1}H-NMR (600 MHz, $CDCl_3$)** δ_H= 88.89 (d, J = 5.1 Hz, 1H), 8.11 (d, J = 6.8 Hz, 2H), 7.88 (d, J = 8.6 Hz, 2H), 7.84 (d, J = 8.3 Hz, 2H), 7.73 (d, J = 8.6 Hz, 2H), 7.67 (dd, J = 5.1, 1.2 Hz, 1H), 7.46 (t, J = 7.4 Hz, 2H), 7.37 (t, J = 7.4 Hz, 2H).**^{13}C-NMR (150 MHz, $CDCl_3$)** δ= 153.29, 152.94, 150.80,

140.26, 138.94, 134.80, 130.87, 129.97, 129.38, 129.16, 128.77, 127.47, 127.17, 126.79, 126.56, 124.70, 121.74, 120.28, 116.91, 115.22, 114.45, 111.22.. **HRMS (ESI) *m/z***; [M+H]+ 463.0183, calc. for $C_{23}H_{16}BrN_2O_2S$ 463.0110.

9-(4-(3-bromophenylsulfonyl)pyridin-2-yl)-9H-carbazole (Br-*m*S4-Py-2Cz)

The title compound was obtained from **9Ac'** (0.6 g, 1.59 mmol) as an off-yellowish colored solid **Br-*m*S4-Py-2Cz** in 55% (0.40 g).

FTIR (KBr, cm^{-1}): 3433, 3060, 2923, 2852, 1597, 1573, 1491, 1479, 1464, 1449, 1407, 1333, 1273, 1243, 1220, 1191, 1159, 1113, 1100, 1079, 992, 965, 909, 845, 798, 784, 768, 749, 719, 707, 674, 658, 617, 605, 593, 563, 527, 491. **^{1}H-NMR (600 MHz, $CDCl_3$)** δ_H= 8.91 (d, J = 5.1 Hz, 1H), 8.17 (s, 1H), 8.13 (d, J = 4.9 Hz, 2H), 8.11 (s, 1H), 7.95 (d, J = 7.9 Hz, 1H), 7.85 (d, J = 8.3 Hz, 2H), 7.79 (d, J = 8.0 Hz, 1H), 7.69 (d, J = 5.1 Hz, 1H), 7.47 (td, J = 8.0, 3.7 Hz, 3H), 7.37 (t, J = 7.4 Hz, 2H). **^{13}C-NMR (150 MHz, $CDCl_3$)** δ= 153.30, 151.62, 151.19, 143.27, 141.47, 139.27, 138.87, 137.43, 136.64, 131.25, 131.01, 127.28, 126.74, 126.68, 124.85, 123.81, 121.99, 120.38, 116.99, 115.38, 114.05. **HRMS (ESI) *m/z***; [M+H]+ 463.0327, calc. for $C_{23}H_{16}BrN_2O_2S$ 463.0110.

General Procedure for Buchwald-Hartwig Reaction

An oven-dried flask was charged with the corresponding halogenated phenyl-sulfonyl pyridine derivative (**9Ac** & **9Ac'**) (1.0 eq), 9H-carbazole (1.1 eq **9Ac** & **9Ac'**) and p-xylene. Then, copper(I)iodide (11% of **9Ac** & **9Ac'**), 1,10-phenanthroline (11% of **9Ac** & **9Ac'**) and potassium carbonate (2.0 eq for **9Ac** & **9Ac'**) were added under nitrogen atmosphere respectively. The reaction mixture was refluxed for 48 h, at 138°C. After cooling to room temperature the mixture was extracted with dichloromethane (3 x 50 mL). The combined organic phases were washed with brine and dried over Na_2SO_4. After the solvent was removed the material was further purified with silica gel column chromatography using dichloromethane:hexane (2:1) eluent.

10-(4-(2-(9H-carbazol-9-yl)pyridin-4-ylsulfonyl)phenyl)-10H-phenothiazine (PTZ-*p*S4-Py-2Cz)

The title compound was obtained from **Br-*p*S4-Py-2Cz** (0.28 g, 0.6 mmol) as white colored solid **PTZ-*p*S4-Py-2Cz** in 78% (0.275 g).

FTIR (KBr, cm^{-1}): 34363434, 3056, 2924, 2851, 1725, 1596, 1573, 1490, 1479, 1452, 1403, 1314, 1275, 1263, 1237, 1191, 1146, 1102, 1028, 1000, 929, 854, 827, 793, 762, 751, 722, 695, 616, 603, 587, 572, 528, 515, 492, 469. **^{1}H-NMR (600 MHz, $CDCl_3$)** δ_H= 8.83 (d, J = 5.1 Hz, 1H), 8.10 (d, J = 7.7 Hz, 2H), 8.05 (s, 1H), 7.83 (d, J = 8.3 Hz, 2H), 7.76 (d, J = 9.0 Hz, 2H), 7.65 (dd, J = 5.1, 1.3 Hz, 1H), 7.49 (d, J = 7.7 Hz, 2H), 7.44 (t, J = 7.1 Hz, 4H), 7.35 (q, J = 7.5 Hz, 4H), 7.28 – 7.20 (m, 3H), 7.09 (d, J = 9.0 Hz, 2H).**^{13}C-NMR (150 MHz, $CDCl_3$)** δ= 153.29, 152.94, 150.80, 140.26, 138.94, 134.80, 130.87, 129.97, 129.38, 129.16, 128.77, 127.47, 127.17, 126.79, 126.56, 124.70, 121.74, 120.28, 116.91, 115.22, 114.45, 111.22. **HRMS (ESI) *m/z***; [M+H]+ 582.1179, calc. for $C_{35}H_{24}N_3O_2S_2$ 582.1304.

10-(3-(2-(9H-carbazol-9-yl)pyridin-4-ylsulfonyl)phenyl)-10H-phenothiazine (PTZ-*m*S4-Py-2Cz)

The title compound was obtained from **Br-*m*S4-Py-2Cz** (0.38 g, 0.82 mmol) as white colored solid **PTZ-*m*S4-Py-2Cz** in 73% (0.35 g).

FTIR (KBr, cm^{-1}): 3435, 3058, 2924, 1598, 1575, 1489, 1462, 1450, 1404, 1327, 1311, 1274, 1260, 1242, 1228, 1190, 1149, 1099, 1076, 1062, 1027, 988, 967, 934, 920, 864, 842, 800, 789, 781, 753, 739, 725, 715, 684, 676, 658, 646, 616, 599, 574, 566, 535, 517, 466.**^{1}H-NMR (600 MHz, $CDCl_3$)** δ_H= 8.89 (d, J = 5.1 Hz, 1H), 8.12 (d, J = 7.6 Hz, 2H), 8.09 (s, 1H), 7.83 (d, J = 8.3 Hz, 3H), 7.81 (d, J = 8.0 Hz, 1H), 7.67 (dd, J = 5.1, 1.1 Hz, 1H), 7.59 (t, J = 7.6 Hz, 1H), 7.49 (d, J = 7.6 Hz, 1H), 7.43 (t, J = 7.3 Hz, 2H), 7.36 (t, J = 7.4 Hz, 2H), 7.24 (d, J = 8.7 Hz, 2H), 7.01 (s, 4H), 6.71 (s, 2H). **^{13}C-NMR (150 MHz, $CDCl_3$)** δ= 153.15, 152.04, 151.03, 141.38, 138.87, 131.28, 127.25, 126.65, 124.80, 123.74, 121.92, 121.44, 120.34, 117.06, 115.36, 111.20. **HRMS (ESI) *m/z***; [M+H]+ 582.1421, calc. for $C_{35}H_{24}N_3O_2S_2$ 582.1304.

2.2. X-ray crystallography

Crystallographic data were recorded on a Bruker APEX II QUAZAR three-circle diffractometer using monchromated Mo-Kα X-radiation (λ = 0.71073 Å). Absorption correction was performed by the multi-scan method implemented in SADABS[20] and space groups were determined using XPREP implemented in APEX2[24]. The structure was solved using the direct methods procedure in SHELXT[25] and refined by full-matrix least squares on F2 using SHELXL[26] in the Olex2 Software Package[27]. All non-hydrogen atoms were refined with anisotropic displacement factors and C-H hydrogen atoms were placed in calculated positions and allowed

to ride on the parent atom. The final geometrical calculations and the molecular drawings were carried out with PLATON[28], MERCURY[29], and DIAMOND (Version 3.1)[30] programs. Structure determinations were deposited with the Cambridge Crystallographic Data Centre with reference CCDC-2089158 and 2089159 for **PTZ-*p*S4-Py-2Cz** and **PTZ-*m*S4-Py-2Cz**, respectively.

2.3. Computational details

Geometry optimizations were performed using the TURBOMOLE V7.5.1[31] quantum chemistry package utilizing the DFT[32,33] with several functionals (B3LYP[34], M06-2X[35], wB97XD[36], CAM-B3LYP[37], and PBE0[38]) and basis sets including 6-31G(d), 6-31G(d,p), TZVP, and aug-cc-pVDZ (aVDZ). The resolution of identity (RI)[39] approximation was used in all relaxations. Time-dependent DFT (TDDFT)[40,41] was employed for the calculation of excited state energies using the relaxed structures at B3LYP/6-31G(d) and B3LYP/aVDZ.

3. Results and Discussion

3.1. Molecular Design and Synthesis

In the previous work, we designed and synthesized differently substituted pyridiyl-sulfonyl derivatives with Cz donors[10]. The best TADF performance was obtained with *para*-substitution of the sulfonyl group by the pyridine ring, with bicarbazole units as donor. In this study, we examine more structurally complex D-aA-D' materials by also introducing a PTZ donor. This is also inspired by previous investigations of asymmetric PTZ-Cz TADF materials, with the additional feature of the asymmetric aA acceptor[16]. PTZ was therefore inserted at the 4- position on the pyridyl-sulfonyl group (*para*-) while Cz was attached at the 2-position on the pyridine ring (**PTZ-*p*S4-Py-2Cz**). An additional isomer was also produced with the PTZ group in a *meta*- position relative to the sulfonyl group (**PTZ-*m*S4-Py-2Cz**). To achieve these 2-carbozyl and 4-phenothiazyl substituted materials, appropriate pyridyl-sulfonyl derivatives were initially produced. Regioselectivity of the C-N bond forming reaction on 2-halogenated pyridine was used to achieve the target structures[42,43]. X-ray and NMR analysis of the final products demonstrates that the first C-N cross-coupling reaction occurred at the 2-position of the regioselective halopyridine.

The synthetic routes and molecular structures are depicted in Scheme 1. The 2,4- substituted pyridiyl-sulfonyl derivatives, **9Ac** & **9Ac'** were synthesized by redox, C-S cross coupling, and oxidation reactions respectively[10]. The target molecules were obtained using *para*- and *meta*-

functionalized aA acceptor units along with appropriate C-N coupling reactions. The first C-N coupling was a copper-catalyzed Ullmann reaction, and the second coupling was a palladium-catalyzed Buchwald-Hartwig reaction. The target materials **PTZ-*p*S4-Py-2Cz** and **PTZ-*m*S4-Py-2Cz** were further characterized by FTIR, NMR (^{1}H- and ^{13}C-), single crystal X-ray, and HRMS, the details of which are shown in ESI (SI-Figure 1-16).

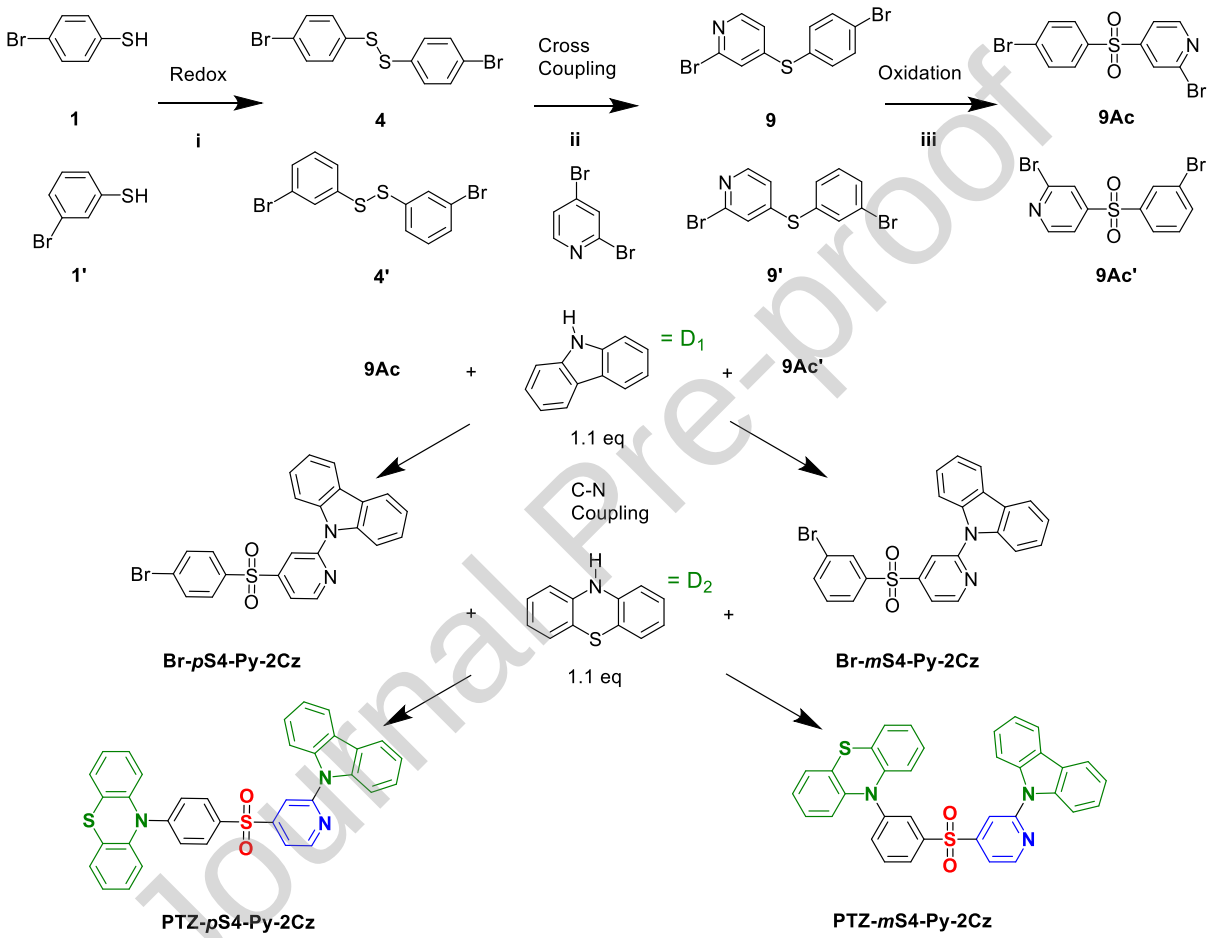

Scheme 1. The synthetic routes of the target molecules

3.2. X-ray single-crystal structure

Single crystals of compounds **PTZ-*p*S4-Py-2Cz** and **PTZ-*m*S4-Py-2Cz** suitable for X-ray measurements were obtained by slow evaporation of a mixture of dichloromethane and methanol (1:1, v/v). Crystallographic parameters are reported in SI-Table 2 and the molecular structures were given in Figure 1. The asymmetric unit of **PTZ-*p*S4-Py-2Cz** contains two crystallographically independent molecules, which are denoted **PTZ-*p*S4-Py-2Cz-A** and **PTZ-*p*S4-Py-2Cz-B** (Figure 1a and 1b). The X-ray structures clearly confirm the identities of the

isomers **PTZ-*p*S4-Py-2Cz** and **PTZ-*m*S4-Py-2Cz**. Selected bond length and angle parameters are given in SI-Table 3.

The orientations of the Cz, PTZ, and pyridyl-sulfone groups were investigated and relevant conformational parameters are given in SI-Table 3. The PTZ unit of **PTZ-*p*S4-Py-2Cz** displayed a slightly less folded donor conformation; the angle between the planes of two benzenes of PTZ was 45.06º for **PTZ-*p*S4-Py-2Cz-A**, 46.05º for **PTZ-*p*S4-Py-2Cz-B** and 50.73º for **PTZ-*m*S4-Py-2Cz** (SI-Figure 22). The **N-C-C-S$_{(PTZ)}$** torsion angles were similar for all structures. Another key detail relevant to the conformation of the PTZ unit is that the sulphur atoms (S_{PTZ}) of the two crystallographically independent molecules of **PTZ-*p*S4-Py-2Cz** had different orientation with respect to the SO_2 group; the S atom was found in *cis*- configuration in **PTZ-*p*S4-Py-2Cz-A** while it was in *trans*- configuration in **PTZ-*p*S4-Py-2Cz-B**. The $S_{(PTZ)}$ atom of compound **PTZ-*m*S4-Py-2Cz** was also oriented in *cis*- configuration.

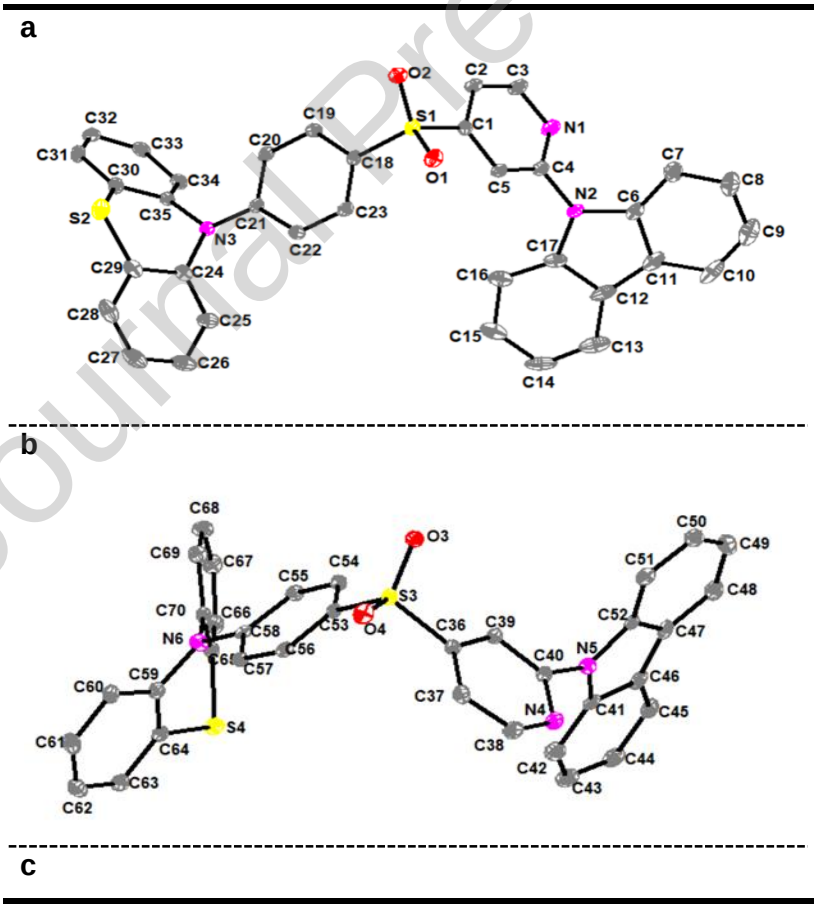

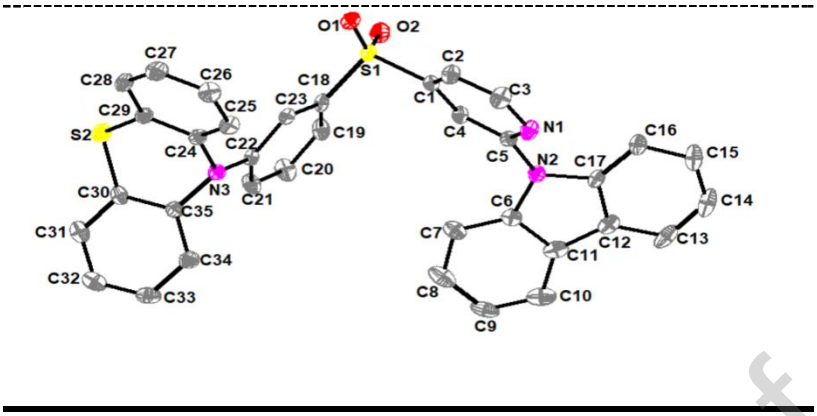

Figure 1. Crystal structures of **a) PTZ-*p*S4-Py-2Cz-A b) PTZ-*p*S4-Py-2Cz-B** and **c) PTZ-*m*S4-Py-2Cz** with atom-numbering scheme. Displacement ellipsoids are drawn at the 30% probability level. The hydrogen atoms have been omitted for clarity.

3.3. Theoretical calculations

A conformational analysis was performed for both **PTZ-*p*S4-Py-2Cz** and **PTZ-*m*S4-Py-2Cz**. For each compound the lowest-energy conformer shown in Figure 2 was obtained following B3LYP/aVDZ relaxation. Vibrational frequency calculations confirmed that the structures shown in Figure 2 are stable, with no vibrational modes possessing imaginary frequencies.

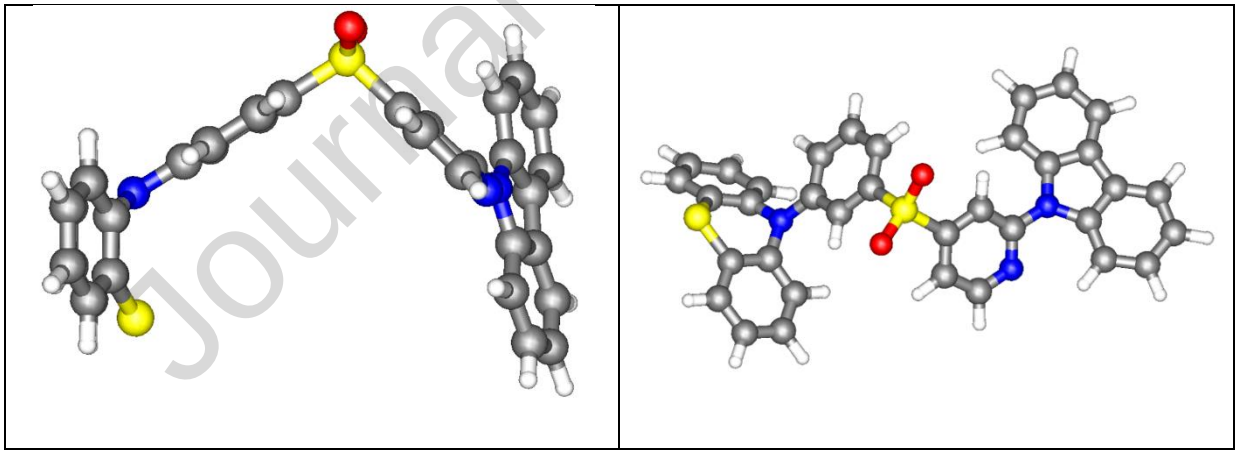

Figure 2. B3LYP/aVDZ optimized geometries of the relaxed **PTZ-*p*S4-Py-2Cz** (left) and **PTZ-*m*S4-Py-2Cz** (right) conformers.

Table 1 lists experimental and computational values of the HOMO, LUMO and band gap energies obtained at several levels of theory. For both molecules, HOMO, LUMO and band gap energies were calculated using both B3LYP/aVDZ and B3LYP/6-31G(d), with the later remaining closer to the experimentally determined values. It should also be mentioned that the

newer hybrid functional of Truhlar and Zhao (M06-2X) and long-range corrected functionals (wB97XD and CAM-B3LYP) overestimate the frontier orbital energies and band gap. Indeed, all calculated HOMO-LUMO gaps are higher than the experimental gaps. However, the calculated optical band gaps (S_0-S_1) at B3LYP/aVDZ and B3LYP/6-31G(d) are in reasonable agreement with experiment, as shown in Table 2.

The lowest singlet (S_1) and triplet (T_1) excited state energies were also calculated using both B3LYP/6-31G(d) and B3LYP/aVDZ methods. Figure 3 shows the electron density distribution of the HOMOs and LUMOs of the singlet and triplet states. In both compounds, while the HOMO is localized on the carbazole donors and slightly extending to the pyridyl bridges, the LUMO is localized on both the sulfone and pyridyl/phenyl rings. However, as shown in Figure 3 we find that the HOMO-1 is also involved in a separate electronic transition. Indeed, the HOMO-1s of both **PTZ-*p*S4-Py-2Cz** and **PTZ-*m*S4-Py-2Cz** are delocalized over the PTZ moiety, raising the possibility of dual CT states associated with the two different donor units. We subsequently observe dual emission in photoluminescence experiments, which we therefore attribute to competing CT emission channels associated with the two different donor units. Independent CT transitions were also observed theoretically and experimentally in similar D-A-D' compounds such as 4-carbazol-10-phenothiazine diphenyl sulfone in previous studies [44,45]. Both S_1 (absorbing at 373 nm, oscillator strength f_{osc} =0.07) and T_1 states (absorbing at 416 nm, f_{osc}=0.32) are mainly π-π* transitions. Table 2 lists the calculated ΔE_{ST}, $\Delta E_{ST(LE)}$, S_1 and T_1 energies of both molecules at B3LYP/6-31G(d) and B3LYP/aVDZ levels of theory. The calculated ΔE_{ST} are between 0.29–0.35 eV, which indicates the possibility of TADF character of these molecules. Moreover, the computed $\Delta E_{ST(LE)}$ (S_1 - T_2 (^{1}CT - ^{3}LE)) are 0.15 eV and 0.21 eV respectively for **PTZ-*p*S4-Py-2Cz** and **PTZ*m*S4-Py-2Cz**.

Table 1. Comparison of experimental and computational HOMO [eV], LUMO [eV] and band gap [eV] energies.

	PTZ-*p*S4-Py-2Cz			**PTZ-*m*S4-Py-2Cz**		
	HOMO	**LUMO**	**E_g**	**HOMO**	**LUMO**	**E_g**
Experiment	-5.14	-1.86	3.28	-5.08	-1.92	3.16
B3LYP/6-31G(d)	-5.49	-1.61	3.88	-5.58	-1.76	3.82
B3LYP/6-31G(d,p)	-5.50	-1.62	3.88	-5.60	-1.76	3.84
B3LYP/TZVP	-5.78	-1.97	3.81	-5.87	-2.13	3.74

B3LYP/aVDZ	-5.82	-2.00	3.82	-5.90	-2.16	3.74
PBE0/aVDZ	-6.00	-1.84	4.16	-6.09	-2.00	4.09
M06-2X/6-31G(d,p)	-6.71	-0.69	6.02	-6.53	-1.18	5.35
wB97XD/6-31G(d,p)	-7.43	0.23	7.66	-7.55	0.05	7.60
CAM-B3LYP/631G(d,p)	-6.79	0.39	6.40	-6.88	-0.54	6.34

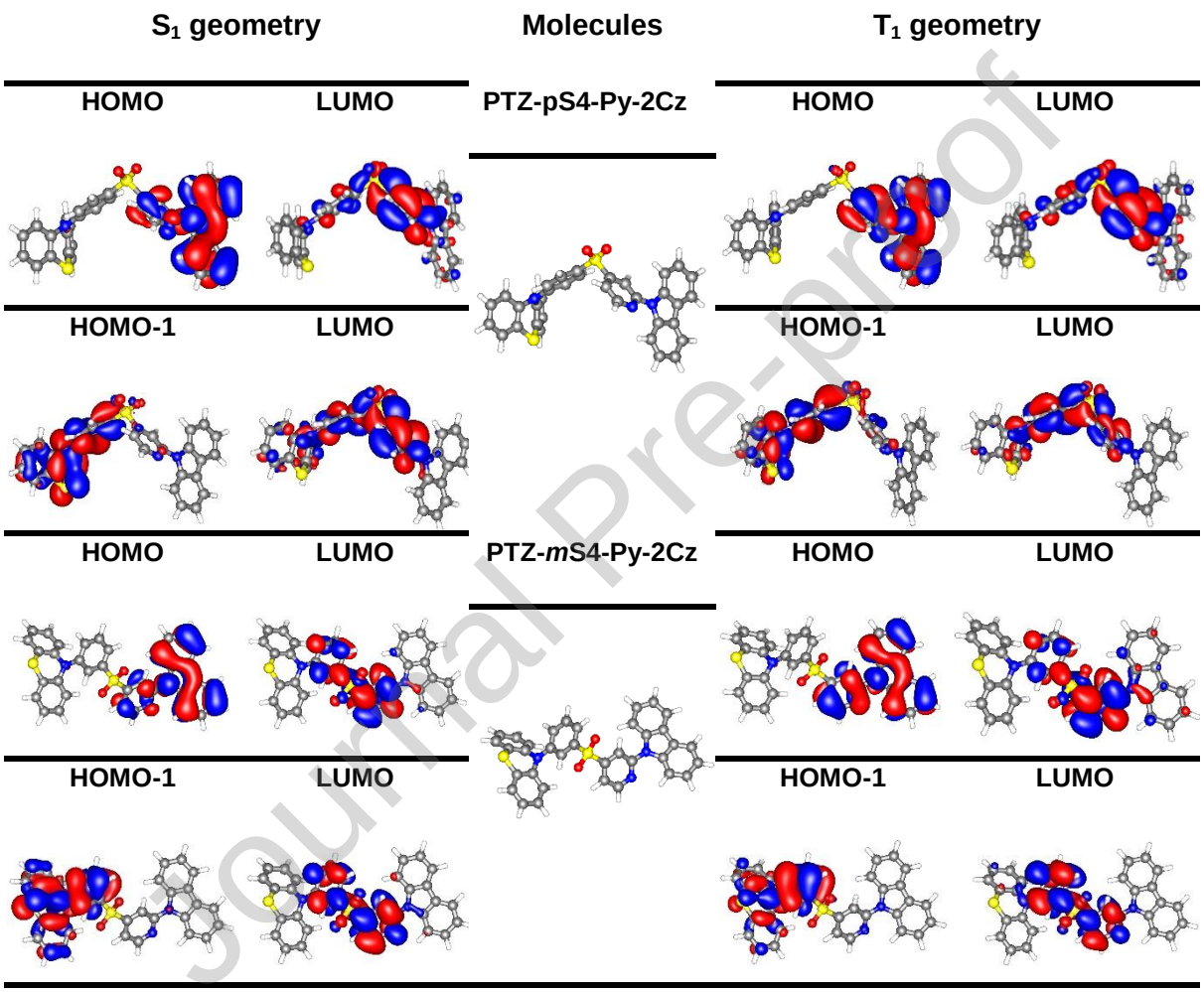

Figure 3. Calculated (B3LYP/aVDZ) natural transition orbitals of the S_1 and T_1 states of **PTZ-*p*S4-Py-2Cz** and **PTZ-*m*S4-Py-2Cz**.

Table 2. Calculated S_1, T_1, ΔE_{ST} (S_1-T_1), $\Delta E_{ST(LE)}$ (S_1-T_2) energies and experimental band gaps (E_g) [eV] for **PTZ-*p*S4-Py-2Cz** and **PTZ-*m*S4-Py-2Cz** conformers at using B3LYP/aVDZ (and B3LYP/6-31G(d) values also provided given in parenthesis).

Molecules	**E_g**	**S_1**	**T_1**	**ΔE_{ST}**	**$\Delta E_{ST(LE)}$**

PTZ-*p*S4-Py-2Cz	3.28	3.26 (3.32)	2.94 (2.97)	0.32 (0.35)	0.15 (0.17)
PTZ-*m*S4-Py-2Cz	3.16	3.19 (3.27)	2.90 (2.94)	0.29 (0.33)	0.21 (0.22)

3.4. Thermal and Electrochemical properties

All measured electrochemical and thermal properties are tabulated in SI-Table 1. The thermal properties of **PTZ-*p*S4-Py-2Cz** and **PTZ-*m*S4-Py-2Cz** were characterized by differential scanning calorimetry (DSC) and thermal gravimetric analysis (TGA) under nitrogen atmosphere. The results of TGA and DSC revealed that the *para*- isomer possesses higher thermal stability than the *meta*- isomer and also sulfonyl group was greatly improved the thermal stability [10,46], as seen in their DSC termograms(SI-Figure 17&18). Compared to the previous Cz-Cz materials, introducing the PTZ group enhances the T_g and T_m [10]. Cyclic voltammetry (CV) measurements were also performed to determine the oxidation potential of the target molecules in degassed acetonitrile solution. The absolute energy levels of emitters were estimated using cyclic voltammetry and UV-visible absorption. The IP/EA energy levels of **PTZ-*p*S4-Py-2Cz** and **PTZ-*m*S4-Py-2Cz** were determined to be -5.14/-1.86 eV and -5.08/-1.92 eV, respectively, measured from the first oxidation wave and relative to ferrocene. Voltammograms showed that the D–Aa–D' molecules exhibited one quasi-reversible and one reversible oxidation (SI-Figure 21).

3.5. Photophysical and TADF properties

In zeonex (1% wt/wt) solid host matrix, the *para*- and *meta*- isomers show structured absorption peaks around 330 nm. The spectra are approximately the sum of the absorption spectra of each D and A components (Figure 4a), which can be attributed to the decoupled nature of donor and acceptor for both Cz and PTZ donors[47]. The photoluminescence spectra of the molecules show dual Gaussian bands in dilute films, with both bands showing positive solvatochromism in different polarity solvents (SI-Figure 19,20). The shorter wavelength gaussian emission band (ca. 425nm) is attributed to the ^{1}CT state of the Cz unit of A−D pair (^{1}CT-Cz), which clearly undergoes a red shift with increasing solvent polarity (Table 3). The second emission band (ca. 550 nm) is attributed to ^{1}CT emission from the PTZ unit of A−D pair (^{1}CT-PTZ), which also shows a clear solvatochromic shift in different polarity solutions and has redshifted emission due to the increased donor strength of PTZ[48]. The ^{1}CT-PTZ band disappears in highly polar solvents like acetonitrile, which we suggest is due to enhanced quenching of this low-energy band due to the energy gap law as its energy becomes too deeply redshifted. None of the molecules shows vibronically structured emission from locally excited singlet states, even in non-polar cyclohexane solution and zeonex polymer host.

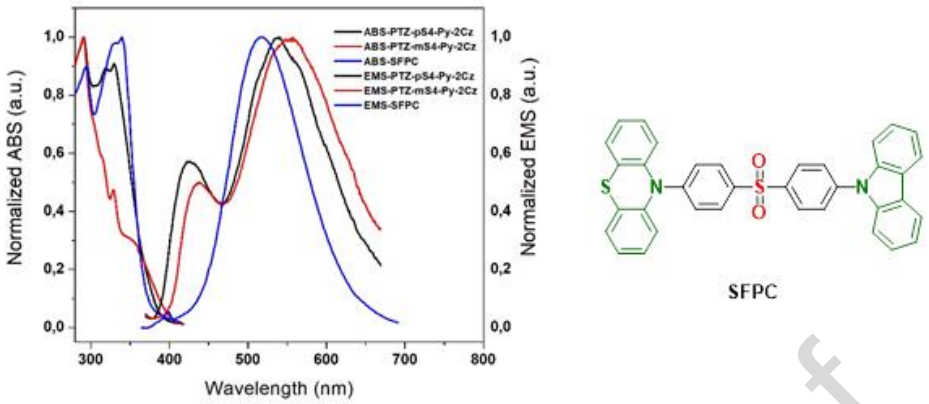

Figure 4. Left Normalized absorption (ABS) and photoluminescence (EMS) spectra of the molecules in zeonex (1% wt/wt) films at RT. **Right** Molecular structure of SFPC.

Table 3. Photophysical properties for **PTZ-*p*S4-Py-2Cz** and **PTZ-*m*S4-Py-2Cz**

Molecules	λ_{PL}[a] (nm)				λ_{ABS}[b] (nm)	PLQY[c] (%)	PLQY[d] (%)	PLQY[e] (%)	ΔE_{ST} (eV)	τ_{PF}[f] (ns)	τ_{DF}[f] (µs)	DF/PF[f]	k_f[g] ($\times 10^7$ s^{-1})	k_{ISC}[g] ($\times 10^7$ s^{-1})	k_{rISC}[g] ($\times 10^5$ s^{-1})
	CH	T	CB	ACN											
PTZ-*p*S4-Py-2Cz	409[i]	444[i]	457[i]	496[i]	283, 320, 329	53	12	20	0.26	7.8	17.2	6.25	1.3	9.9	4.1
	505[ii]	554[ii]	591[ii]	ND											
PTZ-*m*S4-Py-2Cz	428[i]	456[i]	481[i]	507[i]	283, 322, 328	23	3	6	0.33	33.4	37.3	4.64	0.97	2.1	0.95
	524[ii]	563[ii]	ND	ND											

[a] Dual emission maxima in different solvents (Cyclohexane-CH, Toluene-T, Chlorobenzene-CB and Acetonitrile-ACN).

[i] Higher energy emission maximum wavelength attributed to ^{1}CT-Cz [ii] Lower energy emission maximum wavelength attributed to ^{1}CT-PTZ [ND] Peak is not observed in the spectrum.

[b] Absorption maxima for solutions in toluene at RT.

[c] Measured in 1% wt/wt zeonex film under nitrogen atmosphere.

[d] Measured in non-doped solid film under nitrogen atmosphere.

[e] Measured in toluene solution in air.

[f] PF and DF decay lifetimes from weighted averages of biexponential fitting of separate decay regions, with DF/PF ratio from areas of fitted exponentials.

[g] k_f, k_{ISC}, k_{rISC} from simultaneous kinetic fitting of PF and DF emission decays [49].Comparing the optical properties of these materials with a related previously studied linear analog SFPC [16] (Figure 4), we observe dual emission in the pyridine-containing materials while only a single emission peak from the PTZ CT state is observed in SFPC films. This may be explained by the increased conformational freedom of the Cz when adjacent to the pyridine heteroatom, allowing it to explore D-A dihedral angle conformations with higher fluorescence rate, thus activating the ^{1}CT-Cz emissive pathway in the new materials. The CT character of the ^{1}CT-Cz state is also likely enhanced compared to SFPC, due to the adjacent pyridine acting as an auxiliary acceptor[50]. At longer times, all energy is emitted through the lower-energy ^{1}CT-PTZ state (Figure 5, lower contour plots), similar to SFPC, for reasons discussed further below.

The emission spectra redshifts slightly when the positions of PTZ changes from *para*- to *meta*- relative to the sulfone, which also results in a reduction in PLQY values (Table 3). While in zeonex films the PLQY of the *para*- isomer is higher than the meta- isomer (53% compared to 23%), the reported PLQY in the linear SFPC molecule is 93%[51]. This indicates that the structural modifications in **PTZ-*p*S4-Py-2Cz** and **PTZ-*m*S4-Py-2Cz** likely enhance nonradiative pathways, possibly enabled by the flexible PTZ unit. The materials were further analysed using time-resolved spectroscopy in zeonex (1% wt/wt) films, where the complex nature of the emissive states of **PTZ-*p*S4-Py-2Cz, PTZ-*m*S4-Py-2Cz** are determined in more detail. Figure 5 shows the decay of the total integrated emission intensity following pulsed laser excitation of the zeonex films under vacuum at RT and under dry nitrogen gas at 80K. Contour plots of the normalised time-resolved spectra at different times are presented below the decay curves. The materials emit across two distinct time regimes, with prompt fluorescence (PF) occurring over nanoseconds as optically excited CT states emit. Delayed fluorescence (DF) extends over

microseconds as triplet states undergo slower rISC and emit at later times. The PF includes both contribution from the ^{1}CT-Cz and ^{1}CT-PTZ states, where short-lived ^{1}CT-Cz emission is dominant at early times. Long-lived and redshifted ^{1}CT-PTZ emission later significantly dominates the DF decay. By simultaneously fitting the PF and DF regions by kinetic fitting [49], we find that the relevant emission decay constants (k_f, k_{ISC}, and primarily k_{rISC}, Table 3) are improved somewhat compared to the analogous Cz-Cz D-aA-D materials [10]. Similar k_{rISC} values are determined by combining the PLQY and DF/PF ratios using the method described by Dias et al[52]. We take this as confirmation that the amplitude scaling factor "[S_1](t=0)" originally introduced in the kinetic fitting model to account for LE emission in the PF time regime is able to also adequately account for the Cz CT emission.

Nonetheless, for the Cz-PTZ D-aA-D' materials the k_{rISC} rate constants are significantly different for the isomers and improved for the *para*- isomer. We previously found them to be identical in the corresponding Cz-Cz isomers. This finding adds to the growing understanding of how *para*- and *meta*- substitutions can have significant effect on photophysical parameters[11,12,53–56]. In this specific case we suggest that the presence of multiple CT states with distinct rISC pathways leads to an improved overall rate of rISC.

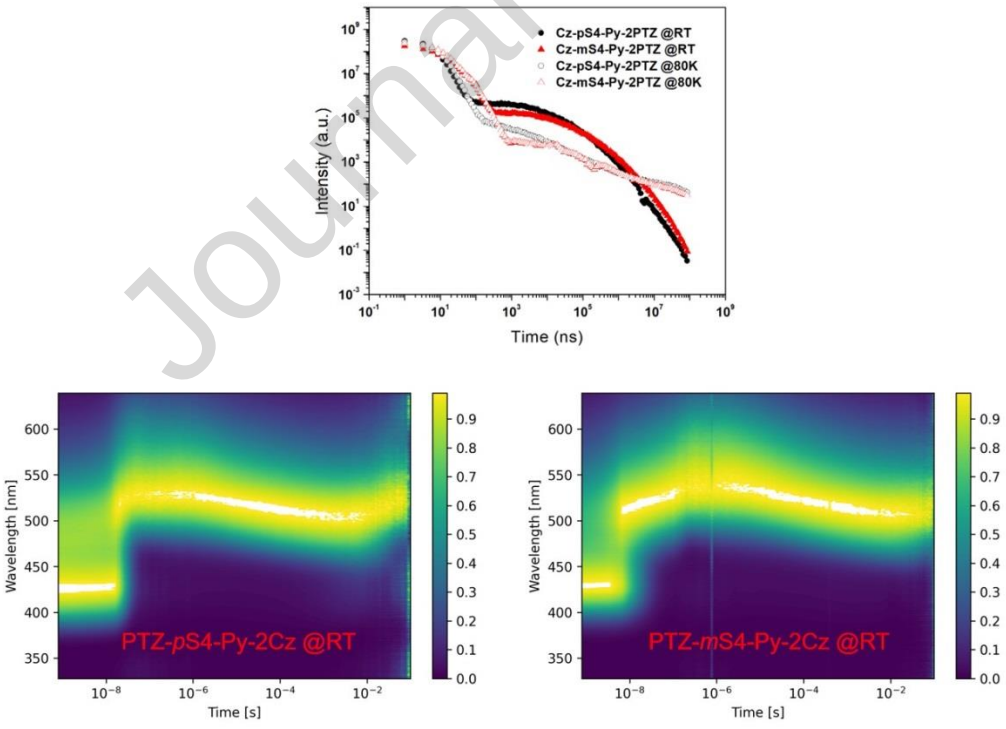

Figure 5. Decay of the total integrated emission intensity for **PTZ-*p*S4-Py-2Cz**, **PTZ-*m*S4-Py-2Cz** in zeonex film (1% wt/wt) at room temperature and at 80K. Below, contour plots of normalised time-resolved emission spectra show how the emission spectra change from ^{1}CT-Cz-dominated at early times, to ^{1}CT-PTZ-dominated at later times.

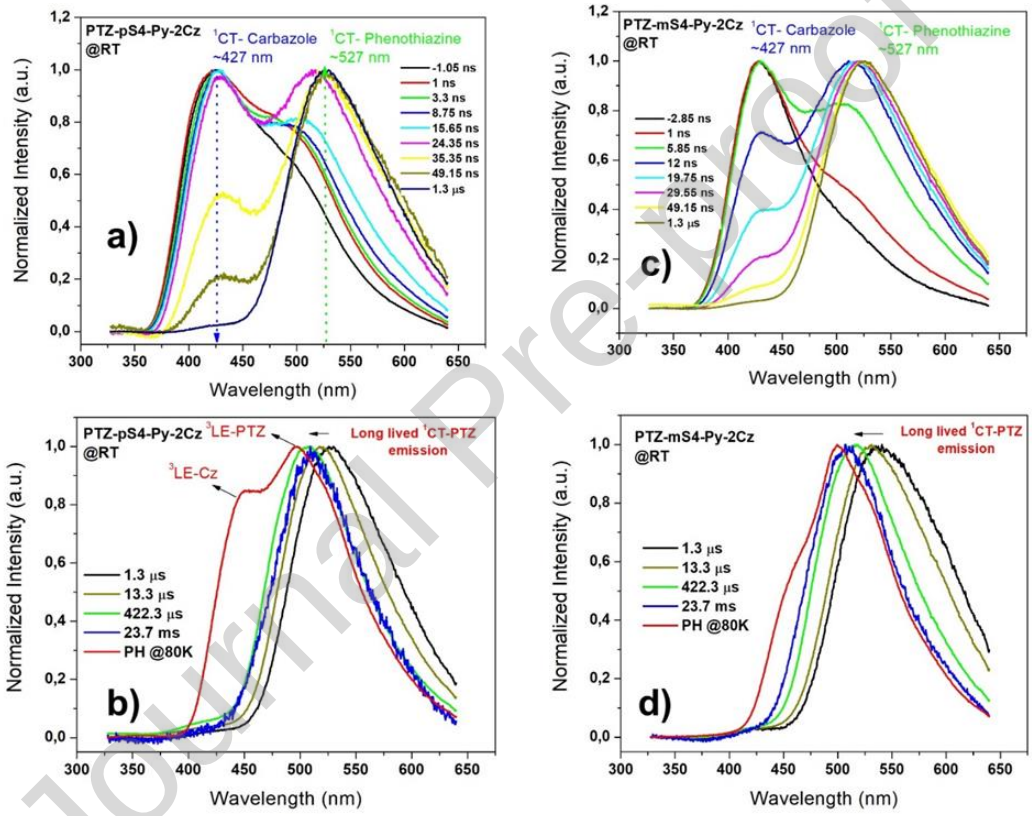

Figure 6. Time-resolved photoluminescence spectra of the molecules in zeonex film (1% wt/wt). **a,c)** Normalized PF (from -1.05 ns to 1.3 µs) spectral evolution at RT **b,d)** Normalized DF (from 1.3 µs to 23.7 ms) spectral evolution at RT. Low temperature phosphorescence specta (PH: 80 K, >10ms delay) is also given for comparison.

The PF and DF spectra show temperature dependent changes, where we observe faster PF decay at RT compared to at 80K. This can be explained under the vibronic coupling theory relevant to D-A TADF emitters, in which both ISC and rISC rates are thermally activated when ΔE_{ST} is small[57]. In the DF, emission from ^{1}CT-PTZ dominates in both of the molecules (Figure 5, similar to in linear SFPC), indicating a more efficient triplet harvesting mechanism in the PTZ

side of the molecules. This outcome is in agreement with the observed ^{1}CT-^{3}LE gaps of the two subunits (see Figure 6b/d), and supported by calculations of the same (0.22 eV and 0.28 eV respectively at B3LYP/6-31G(d) and B3LYP/aVDZ levels of theory). Finally, when the PTZ group is shifted from *para*- to *meta*-, the DF intensity and rate of rISC both decrease alongside significant decrease in PLQY (Table 3). As seen previously[10,12], this *meta*- positioning of D and A units decreases the electronic coupling between them. Since PTZ is the donor unit primarily involved in the ^{1}CT-PTZ DF emission, its position therefore significantly controls the DF properties. Nonetheless, the active emission from both Cz and PTZ CT states stands in contrast to other similar materials such as SPFC, and the enhanced rISC is likely assisted by the presence of multiple rISC pathways.

3.6. Electroluminescent properties

OLED Device Fabrication:

Non-doped bottom-emitting OLEDs were investigated for both materials, using a stack structure of ITO/NPB(50 nm)/synthesized molecules(20nm)/TPBi (30 nm)/LiF (1 nm)/Al (100 nm). The energy levels of this stack are shown in SI-Figure 26. Pre-patterned indium tin oxide coated glass (ITO, 120 nm, Kintec Company) with a sheet resistance of 10 Ω·square-1 was used as the substrate. These substrates were cleaned with distilled water, acetone, ethanol, and isopropanol in an ultrasonic solvent bath, and treated with oxygen plasma for 5 min before use. N,N′-Di(1-naphthyl)-N,N′-diphenyl-(1,1′-biphenyl)-4,4′-diamine (NPB, Sigma-Aldrich) was deposited in an evaporation chamber under high vacuum (pressure below 1×10−6 mBar) as the hole injection layer (50 nm). Next, emissive layers of PTZ-pS4-Py-2Cz or PTZ-mS4-Py-2Cz (20 nm), electron transport layer of 1,3,5-tris(phenyl-2-benzimidazolyl)benzene (TPBI, 30 nm), and a cathode composed of calcium (10 nm) and aluminium (100 nm) were sequentially deposited via evaporation. The size of the active OLED area defined by shadow masks was 9 mm^{2}. The electroluminescence spectra and current density–voltage-brightness of the devices were measured with a Hamamatsu PMA-12 C10027 Photonic Multichannel analyzer and digital multimeter (2427-C 3A Keithley). All the measurements were carried out at room temperature under ambient conditions.

OLED Device Results:

As can be seen from Figure 7, the **PTZ-*p*S4-Py-2Cz** OLED showed a maximum luminous efficiency of 4.5 cd/A, and 1.5 cd/A for the **PTZ-*m*S4-Py-2Cz** OLED. The maximum luminescence were about 450 and 350 cd/m^{-2} for the *para*- and *meta*- materials respectively, although with significantly higher turn-on and operating voltages for *para*-. Figure 7d shows the

EL spectra of the OLEDs, which exhibited yellow emissions at 580 and 560 nm for the *para*- and the *meta*- respectively, with other optoelectronic data summarised in Table 4. The higher relative performance of the **PTZ-*p*S4-Py-2Cz** device is in great agreement with optical findings. Indeed, the lower conductivity of the *para*- substituted material is evident in Figure 7a, which may in turn have led to better charge confinement in the emissive layer than with the more conductive *meta*-substituted material.

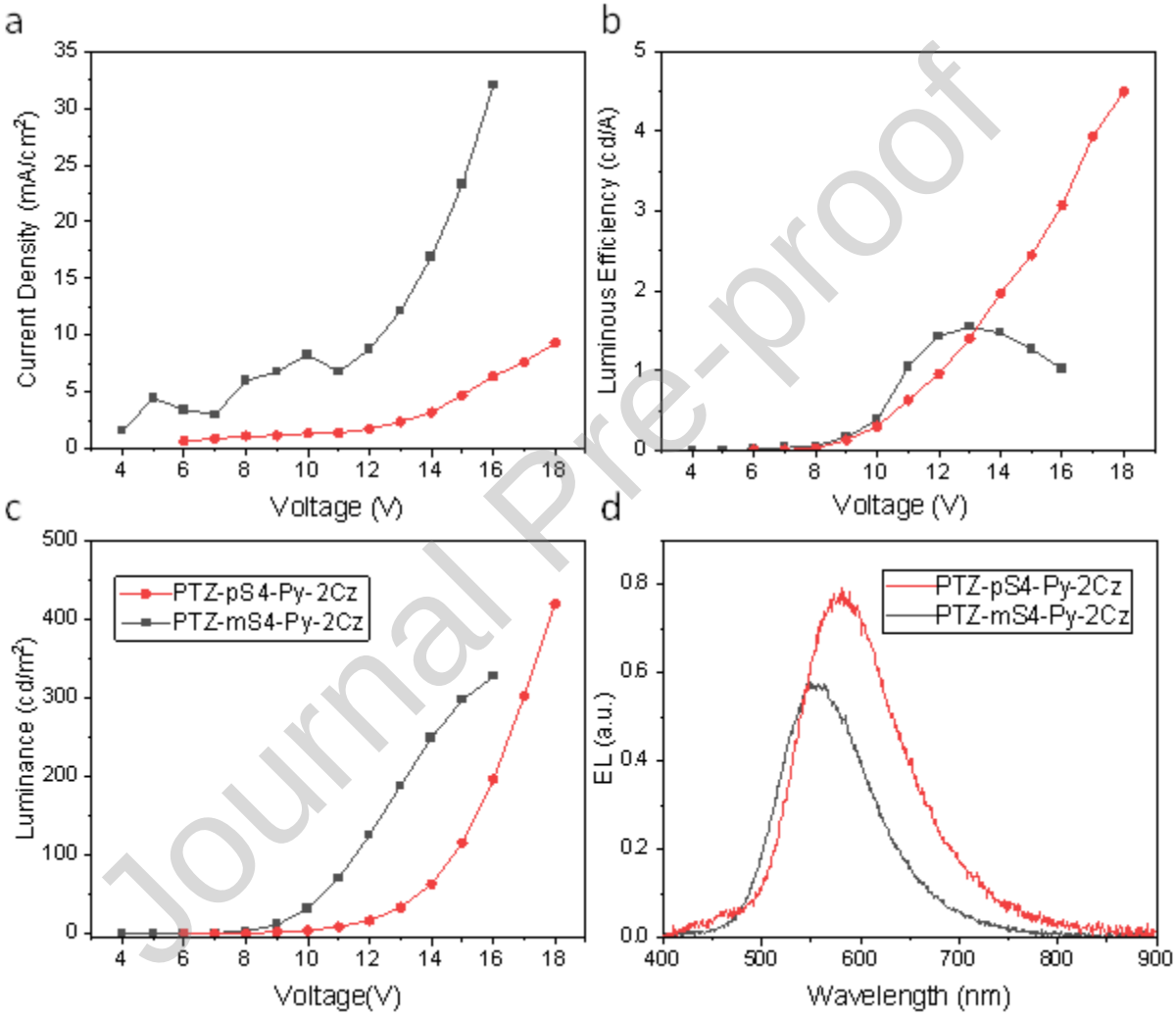

Figure 7. a) Current density–Voltage, **b)** Luminous efficiency–Voltage of **c)** Luminance–Voltage and **d)** Electroluminescence (EL) characteristics of OLEDs fabricated with **PTZ-*p*S4-Py-2Cz** and **PTZ-*m*S4-Py-2Cz.**

Table 4. Summary of device characteristics: Turn-on voltage (V_{ON}), luminous efficiency (LE), maximum external quantum efficiency (EQE), color coordinates and EL wavelength(λ_{EL})

Sample	V_{ON} (V)[a]	LE (cd/A)[b]	EQE_{max} (%)[b]	Color Coordinates (x;y)[c]	λ_{EL} (nm)[b]
PTZ-*p*S4-Py-2Cz	8	4.5	1.9	0.49; 0.48	580
PTZ-*m*S4-Py-2Cz	7	1.5	0.5	0.41; 0.53	560

[a] Turn-on voltage at 1 cd/m^2.

[b] Maximum values.

[c] Chromaticity coordinates (CIE 1931) recorded at 12 V.

Conclusion:

In conclusion, we have investigated the emissive properties of 2,4-substituted pyridyl-sulfonyl based regioisomers. The multistep synthesis of the Cz and PTZ substituted compounds was confirmed by single crystal X-ray and NMR analysis. The HOMO and LUMOs for both molecules have spatial separation, with the HOMO localized on Cz, HOMO-1 on PTZ, and LUMO across the sulfone and pyridyl/phenyl rings. Changes in the position of PTZ from *para*- to *meta*- leads to considerable detrimental impacts on TADF and PLQY properties, in contrast to analogous Cz-Cz materials which had no strong isomeric differences. Prompt emission is dominated by the ^{1}CT-PTZ state, and delayed emission arises from the ^{1}CT-PTZ state leading to steady-state dual emission in both materials. Non-doped OLEDs based on **PTZ-*m*S4-Py-2Cz** & **PTZ-*p*S4-Py-2Cz** present warm-yellowish emission with CIE coordinates of (0.41; 0.53, 0.49; 0.48), and maximum EQEs of 0.5% and 1.9%, respectively.

Acknowledgements

The authors would like thank the Turkish State Planning Association for financial support.

References

[1] H. Uoyama, K. Goushi, K. Shizu, H. Nomura, C. Adachi, Highly efficient organic light-emitting diodes from delayed fluorescence, (2012). https://doi.org/10.1038/nature11687.

[2] H. Nakanotani, T. Higuchi, T. Furukawa, K. Masui, K. Morimoto, M. Numata, H. Tanaka, Y. Sagara, T. Yasuda, C. Adachi, ARTICLE High-efficiency organic light-emitting diodes with fluorescent emitters, Nat. Commun. (2014). https://doi.org/10.1038/ncomms5016.

[3] C.E. green thermally activated delayed fluorescence (TADF) from a phenoxazine-triphenyltriazine (PXZ–TRZ) derivative Tanaka, Hiroyuki ; Shizu, Katsuyuki; Miyazakia, Hiroshi; Adachi, Chemical Communications, Chem. Commun. 48 (2012) 11369–11468.

https://doi.org/10.1039/c2cc36237f.

[4] Q. Peng, W. Li, S. Zhang, P. Chen, F. Li, Y. Ma, Evidence of the Reverse Intersystem Crossing in Intra-Molecular Charge-Transfer Fluorescence-Based Organic Light-Emitting Devices Through Magneto-Electroluminescence Measurements, Adv. Opt. Mater. 1 (2013) 362–366. https://doi.org/10.1002/ADOM.201300028.

[5] A. Endo, K. Sato, K. Yoshimura, T. Kai, A. Kawada, H. Miyazaki, C. Adachi, Efficient up-conversion of triplet excitons into a singlet state and its application for organic light emitting diodes, Appl. Phys. Lett. 98 (2011) 083302. https://doi.org/10.1063/1.3558906.

[6] S.Y. Lee, T. Yasuda, H. Nomura, C. Adachi, High-efficiency organic light-emitting diodes utilizing thermally activated delayed fluorescence from triazine-based donor–acceptor hybrid molecules, Appl. Phys. Lett. 101 (2012) 093306. https://doi.org/10.1063/1.4749285.

[7] G. Méhes, H. Nomura, Q. Zhang, T. Nakagawa, C. Adachi, Enhanced Electroluminescence Efficiency in a Spiro-Acridine Derivative through Thermally Activated Delayed Fluorescence, Angew. Chemie Int. Ed. 51 (2012) 11311–11315. https://doi.org/10.1002/ANIE.201206289.

[8] K. Kawasumi, T. Wu, T. Zhu, H.S. Chae, T. Van Voorhis, M.A. Baldo, T.M. Swager, Thermally Activated Delayed Fluorescence Materials Based on Homoconjugation Effect of Donor–Acceptor Triptycenes, J. Am. Chem. Soc. 137 (2015) 11908–11911. https://doi.org/10.1021/JACS.5B07932.

[9] R. Furue, T. Akuro Nishimoto + ,I Nseob Park, J. Lee, T. Yasuda, Organic Light-Emitting Diodes Aggregation-Induced Delayed Fluorescence Based on Donor/ Acceptor-Tethered Janus Carborane Triads:Unique Photophysical Properties of Nondoped OLEDs, (n.d.). https://doi.org/10.1002/ange.201603232.

[10] G. Haykir, M. Aydemir, A. Danos, S. Gumus, G. Hizal, A.P. Monkman, F. Turksoy, Effects of asymmetric acceptor and donor positioning in deep blue pyridyl-sulfonyl based TADF emitters, Dye. Pigment. 194 (2021) 109579. https://doi.org/10.1016/J.DYEPIG.2021.109579.

[11] I.A. Wright, A. Danos, S. Montanaro, A.S. Batsanov, A.P. Monkman, M.R. Bryce, Conformational Dependence of Triplet Energies in Rotationally Hindered N- and S-Heterocyclic Dimers: New Design and Measurement Rules for High Triplet Energy OLED Host Materials, Chem. - A Eur. J. 27 (2021) 6545–6556. https://doi.org/10.1002/chem.202100036.

[12] N.A. Kukhta, H.F. Higginbotham, T. Matulaitis, A. Danos, A.N. Bismillah, N. Haase, M.K.

Etherington, D.S. Yufit, P.R. McGonigal, J.V. Gražulevičius, A.P. Monkman, Revealing resonance effects and intramolecular dipole interactions in the positional isomers of benzonitrile-core thermally activated delayed fluorescence materials, J. Mater. Chem. C. 7 (2019) 9184–9194. https://doi.org/10.1039/c9tc02742d.

[13] A. Danos, D. Gudeika, N. A. Kukhta, R. Lygaitis, M. Colella, H. F. Higginbotham, A. N. Bismillah, P. R. McGonigal, J. V. Grazulevicius, A. P. Monkman, Not the sum of their parts: understanding multi-donor interactions in symmetric and asymmetric TADF emitters, J. Mater. Chem. C, (2022), Advanced Article. https://doi.org/10.1039/D1TC04171A.

[14] R. Pashazadeha, G. Sycha, S. Nasiria, K. Leitonasa, A. Lazauskas, D. Volyniuka, P.J. Skabarac, J.V. Grazuleviciusa, Multifunctional asymmetric D-A-D' compounds: Mechanochromic luminescence, thermally activated delayed fluorescence and aggregation enhanced emission, Chemical Engineering Journal. 401 (2020) 401 (2020) 125962. https://doi.org/10.1016/j.cej.2020.125962.

[15] P. Arsenyan, B. Vigante, K. Leitonas, D. Volyniuk, V. Andruleviciene, L. Skhirtladze, S. Belyakova, J. V. Grazulevicius, Dual versus normal TADF of pyridines ornamented with multiple donor moieties and their performance in OLEDs, J. Phys. Chem. C. 9 (2021) 3928-3938. https://doi.org/10.1039/D0TC05745B.

[16] M. Aydemir, S. Xu, C. Chen, M.R. Bryce, Z. Chi, A.P. Monkman, Photophysics of an Asymmetric Donor-Acceptor-Donor′ TADF Molecule and Reinterpretation of Aggregation-Induced TADF Emission in These Materials, J. Phys. Chem. C. 121 (2017) 17764–17772. https://doi.org/10.1021/acs.jpcc.7b06299.

[17] S.M. Sartor, C.H. Chrisman, R.M. Pearson, G.M. Miyake, N.H. Damrauer, Designing High-Triplet-Yield Phenothiazine Donor−Acceptor Complexes for Photoredox Catalysis, J. Phys. Chem. A. 124 (2020) 24. https://doi.org/10.1021/acs.jpca.9b10400.

[18] M. Sailer, M. Nonnenmacher, T. Oeser, T.J.J. Müller, Synthesis and Electronic Properties of 3-Acceptor-Substituted and 3,7-Bisacceptor-Substituted Phenothiazines, European J. Org. Chem. 2006 (2006) 423–435. https://doi.org/10.1002/EJOC.200500539.

[19] B. Huang, W.-C. Chen, Z. Li, J. Zhang, W. Zhao, Y. Feng, B.Z. Tang, C.-S. Lee, Manipulation of Molecular Aggregation States to Realize Polymorphism, AIE, MCL, and TADF in a Single Molecule, Angew. Chemie. 130 (2018) 12653–12657. https://doi.org/10.1002/ANGE.201806800.

[20] C. Chen, R. Huang, A.S. Batsanov, P. Pander, Y.-T. Hsu, Z. Chi, F.B. Dias, M.R. Bryce, Intramolecular Charge Transfer Controls Switching Between Room Temperature

Phosphorescence and Thermally Activated Delayed Fluorescence, Angew. Chemie Int. Ed. 57 (2018) 16407–16411. https://doi.org/10.1002/ANIE.201809945.

[21] R. Huang, J.S. Ward, N.A. Kukhta, J. Avó, J. Gibson, T. Penfold, J.C. Lima, A.S. Batsanov, M.N. Berberan-Santos, M.R. Bryce, F.B. Dias, The influence of molecular conformation on the photophysics of organic room temperature phosphorescent luminophores, J. Mater. Chem. C. 6 (2018) 9238–9247. https://doi.org/10.1039/C8TC02987C.

[22] N. Hasan, Z. Ma, J. Liu, Z. Li, C. Qian, Y. Liu, M. Chen, H. Jiang, X. Jia, Z. Ma, Selective Expression of a Carbazole-Phenothiazine Derivative Leads to Dual-mode AIEE, TADF and Distinctive Mechanochromism, ChemPhysChem. (2021). https://doi.org/10.1002/CPHC.202100435.

[23] 2014) SADABS, version 2014/5, Bruker (Bruker AXS Inc., Madison, WI, No Title, (n.d.).

[24] 2014). APEX2, version 2014.11-0, Bruker (Bruker AXS Inc., Madison, WI, No Title, (n.d.).

[25] G.M. Sheldrick, SHELXT - Integrated space-group and crystal-structure determination, Acta Crystallogr. Sect. A Found. Crystallogr. 71 (2015) 3–8. https://doi.org/10.1107/S2053273314026370.

[26] G.M. Sheldrick, Crystal structure refinement with SHELXL, Acta Crystallogr. Sect. C Struct. Chem. 71 (2015) 3–8. https://doi.org/10.1107/S2053229614024218.

[27] O. V. Dolomanov, L.J. Bourhis, R.J. Gildea, J.A.K. Howard, H. Puschmann, OLEX2: A complete structure solution, refinement and analysis program, J. Appl. Crystallogr. 42 (2009) 339–341. https://doi.org/10.1107/S0021889808042726.

[28] A.L. Spek, Structure validation in chemical crystallography, Acta Crystallogr. Sect. D Biol. Crystallogr. 65 (2009) 148–155. https://doi.org/10.1107/S090744490804362X.

[29] C.F. Macrae, P.R. Edgington, P. McCabe, E. Pidcock, G.P. Shields, R. Taylor, M. Towler, J. Van De Streek, Mercury: Visualization and analysis of crystal structures, J. Appl. Crystallogr. 39 (2006) 453–457. https://doi.org/10.1107/S002188980600731X.

[30] B. K., (No Title), (n.d.). https://www.crystalimpact.com/download/diamond/demo/Readme.txt (accessed June 21, 2021).

[31] S.G. Balasubramani, G.P. Chen, S. Coriani, M. Diedenhofen, M.S. Frank, Y.J. Franzke, F. Furche, R. Grotjahn, M.E. Harding, C. Hättig, A. Hellweg, B. Helmich-Paris, C. Holzer, U. Huniar, M. Kaupp, A. Marefat Khah, S. Karbalaei Khani, T. Müller, F. Mack, B.D. Nguyen, S.M. Parker, E. Perlt, D. Rappoport, K. Reiter, S. Roy, M. Rückert, G. Schmitz, M. Sierka, E. Tapavicza, D.P. Tew, C. Van Wüllen, V.K. Voora, F. Weigend, A. Wodyński,

J.M. Yu, TURBOMOLE: Modular program suite for ab initio quantum-chemical and condensed-matter simulations, J. Chem. Phys. 152 (2020) 184107. https://doi.org/10.1063/5.0004635.

[32] P. Hohenberg, W. Kohn, Inhomogeneous electron gas, Phys. Rev. 136 (1964) B864. https://doi.org/10.1103/PhysRev.136.B864.

[33] W. Kohn, L.J. Sham, Self-consistent equations including exchange and correlation effects, Phys. Rev. 140 (1965) A1133. https://doi.org/10.1103/PhysRev.140.A1133.

[34] A.D. Becke, Density-functional thermochemistry. III. The role of exact exchange, J. Chem. Phys. 98 (1993) 5648–5652. https://doi.org/10.1063/1.464913.

[35] Y. Zhao, D.G. Truhlar, The M06 suite of density functionals for main group thermochemistry, thermochemical kinetics, noncovalent interactions, excited states, and transition elements: Two new functionals and systematic testing of four M06-class functionals and 12 other function, Theor. Chem. Acc. 120 (2008) 215–241. https://doi.org/10.1007/s00214-007-0310-x.

[36] J. Da Chai, M. Head-Gordon, Long-range corrected hybrid density functionals with damped atom-atom dispersion corrections, Phys. Chem. Chem. Phys. 10 (2008) 6615–6620. https://doi.org/10.1039/b810189b.

[37] T. Yanai, D.P. Tew, N.C. Handy, A new hybrid exchange-correlation functional using the Coulomb-attenuating method (CAM-B3LYP), Chem. Phys. Lett. 393 (2004) 51–57. https://doi.org/10.1016/j.cplett.2004.06.011.

[38] C. Adamo, V. Barone, Toward reliable density functional methods without adjustable parameters: The PBE0 model, J. Chem. Phys. 110 (1999) 6158–6170. https://doi.org/10.1063/1.478522.

[39] K. Eichkorn, O. Treutler, H. Öhm, M. Häser, R. Ahlrichs, Auxiliary basis sets to approximate Coulomb potentials, Chem. Phys. Lett. 240 (1995) 283–290. https://doi.org/10.1016/0009-2614(95)00621-A.

[40] E. Runge, E.K.U. Gross, Density-functional theory for time-dependent systems, Phys. Rev. Lett. 52 (1984) 997–1000. https://doi.org/10.1103/PhysRevLett.52.997.

[41] E.K.U. Gross, W. Kohn, Time-dependent density-functional theory, Adv. Quantum Chem. 21 (1990) 255–291. https://doi.org/10.1016/S0065-3276(08)60600-0.

[42] C. Sicre, J.L. Alonso-Gómez, M.M. Cid, Regioselectivity in alkenyl(aryl)-heteroaryl Suzuki cross-coupling reactions of 2,4-dibromopyridine. A synthetic and mechanistic study, Tetrahedron. 62 (2006) 11063–11072. https://doi.org/10.1016/j.tet.2006.09.040.

[43] S. Schröter, C. Stock, T. Bach, Regioselective cross-coupling reactions of multiple

halogenated nitrogen-, oxygen-, and sulfur-containing heterocycles, Tetrahedron. 61 (2005) 2245–2267. https://doi.org/10.1016/j.tet.2004.11.074.

[44] B. Xu,Y. Mu, Z. Mao, Z. Xie, H. Wu, Y. Zhang, C. Jin, Z. Chi, S. Liu, J. Xu, Y.-C. Wu, P.-Y. Lu, A. Lienc, M. R. Bryce, Achieving remarkable mechanochromism and white-light emission with thermally activated delayed fluorescence through the molecular heredity principle, Chem. Sci. 7 (2016) 2201-2206. https://doi.org/10.1039/C5SC04155D.

[45] W. Wei , Z. Yang, X. Chen, T. Liu , Z. Mao, J. Zhao, Z. Chi, Modulation of π-linkers in asymmetric thermally activated delayed fluorescence molecules enabling high performanceOLEDs, J. Mater. Chem. C. 8 (2020) 3663-3668. DOI: 10.1039/C9TC06608J.

[46] D. Zhong, Y. Yu, L. Yue, X. Yang, L. Ma, G. Zhou, Z. Wu, Optimizing molecular rigidity and thermally activated delayed fluorescence (TADF) behavior of phosphoryl center π-conjugated heterocycles-based emitters by tuning chemical features of the tether groups, Chem. Eng. J. 413 (2021) 127445. https://doi.org/10.1016/j.cej.2020.127445.

[47] Z. Xie, C. Chen, S. Xu, J. Li, Y. Zhang, S. Liu, J. Xu, Z. Chi, White-Light Emission Strategy of a Single Organic Compound with Aggregation-Induced Emission and Delayed Fluorescence Properties, Angew. Chemie. 127 (2015) 7287–7290. https://doi.org/10.1002/ANGE.201502180.

[48] J.S. Ward, A. Danos, P. Stachelek, M.A. Fox, A.S. Batsanov, A.P. Monkman, M.R. Bryce, Exploiting trifluoromethyl substituents for tuning orbital character of singlet and triplet states to increase the rate of thermally activated delayed fluorescence, Mater. Chem. Front. 4 (2020) 3602–3615. https://doi.org/10.1039/d0qm00429d.

[49] N. Haase, A. Danos, C. Pflumm, A. Morherr, P. Stachelek, A. Mekic, W. Brütting, A.P. Monkman, Kinetic Modeling of Transient Photoluminescence from Thermally Activated Delayed Fluorescence, J. Phys. Chem. C. 122 (2018) 29173–29179. https://doi.org/10.1021/acs.jpcc.8b11020.

[50] L. Salah, M.K. Etherington, A. Shuaib, A. Danos, A.A. Nazeer, B. Ghazal, A. Prlj, A.T. Turley, A. Mallick, P.R. McGonigal, B.F.E. Curchod, A.P. Monkman, S. Makhseed, Suppressing dimer formation by increasing conformational freedom in multi-carbazole thermally activated delayed fluorescence emitters, J. Mater. Chem. C. 9 (2021) 189–198. https://doi.org/10.1039/d0tc04222f.

[51] C. Li, X. Fan, C. Han, H. Xu, A ternary phosphine oxide host featuring thermally activated delayed fluorescence for blue PHOLEDs with >20% EQE and extremely low roll-offs, J. Mater. Chem. C. 6 (2018) 6747–6754. https://doi.org/10.1039/c8tc02010h.

[52] F. B. Dias, T. J. Penfold, A.P. Monkman, Photophysics of thermally activated delayed fluorescence molecules, Methods Appl. Fluoresc., 5 (2017) 012001. https://doi.org/10.1088/2050-6120/aa537e.

[53] P. Stachelek, J.S. Ward, P.L. Dos Santos, A. Danos, M. Colella, N. Haase, S.J. Raynes, A.S. Batsanov, M.R. Bryce, A.P. Monkman, Molecular Design Strategies for Color Tuning of Blue TADF Emitters, ACS Appl. Mater. Interfaces. 11 (2019) 27125–27133. https://doi.org/10.1021/acsami.9b06364.

[54] D.C. G A Pinto, C.M. M Santos, A.M. S Silva, Trivandrum-695 023, Kerala, India Recent Research Developments in Heterocyclic Chemistry, 2007.

[55] D. Hall, K. Stavrou, E. Duda, A. Danos, S. Bagnich, S. Warriner, A.M.Z. Slawin, D. Beljonne, A. Köhler, A. Monkman, Y. Olivier, E. Zysman-Colman, Diindolocarbazole – Achieving Multiresonant Thermally Activated Delayed Fluorescence Without The Need for Acceptor Units, (2021). https://doi.org/10.1039/D1MH01383A.

[56] J. Wei, C. Zhang, D. Zhang, Y. Zhang, Z. Liu, Z. Li, G. Yu, L. Duan, C. Zhang, D. Zhang, Y.W. Zhang, Z.Y. Liu, L. Duan, J. Wei, G. Yu, Z. Li, Indolo[3,2,1-jk]carbazole Embedded Multiple-Resonance Fluorophors for Narrowband Deep-blue Electroluminescence with EQE≈34.7 % and CIEy≈0.085, Angew. Chemie Int. Ed. 60 (2021) 12269–12273. https://doi.org/10.1002/ANIE.202017328.

[57] T.J. Penfold, On Predicting the Excited-State Properties of Thermally Activated Delayed Fluorescence Emitters, (2015). https://doi.org/10.1021/acs.jpcc.5b03530.

Author Contributions

G.H., G.H. and F.T. synthesized the materials and performed the chemical analysis. A.T. carried out the DFT calculations. M.A. performed all photophysical measurements. M.A. and A.D. analyzed the photophysical data. A.P.M. help to interpret the data. E.T. fabricated and characterized OLED. F.Y. refined the single crystal data and performed structural analysis. G.H, F.T., M.A., A.D., A.T, E.T and F.Y. prepared the manuscript. All authors have given approval to the final version of the manuscript.

Declaration of interests

☒ The authors declare that they have no known competing financial interests or personal relationships that could have appeared to influence the work reported in this paper.

☐The authors declare the following financial interests/personal relationships which may be considered as potential competing interests:

Highlights:

- We report the synthesis and structural characterization of D-aA-D' type pyridyl-sulfonyl based isomers comprising the phenothiazine and carbazole donor units, which are able to emit thermally activated delayed fluorescence
- The isomer with *para*- phenothiazine group displays significantly improved delayed fluorescence and emission quantum yields
- Both materials exhibit warm-yellowish emission in non-doped OLEDs with CIE coordinates of (0.41; 0.53, 0.49; 0.48) and maximum EQEs of 0.5% (*meta*- isomer) and 1.9% (*para*- isomer)